Applied Catalysis B: Environmental 152–153 (2014) 328–334

Contents lists available at ScienceDirect

Applied Catalysis B: Environmental

journal homepage: www.elsevier.com/locate/apcatb

Excellent photocatalytic activity of Yb^{3+}, Er^{3+} co-doped $BiVO_4$ photocatalyst

S. Obregón, G. Colón*

Instituto de Ciencia de Materiales de Sevilla, Centro Mixto CSIC-Universidad de Sevilla, C/Américo Vespucio 49, 41092 Sevilla, Spain

ARTICLE INFO

Article history:
Received 28 November 2013
Received in revised form 22 January 2014
Accepted 27 January 2014
Available online 2 February 2014

Keyword:
Erbium
Ytterbium
$BiVO_4$
Photocatalysis
Up-conversion
Methylene Blue
O_2 evolution

ABSTRACT

Ytterbium-Erbium co-doped $BiVO_4$ have been synthesized by means of a surfactant free hydrothermal method having good photoactivities under sun-like excitation for the degradation of *Methylene Blue* and O_2 evolution reactions. From the structural and morphological characterization it has been stated that the presence of Yb^{3+} and Er^{3+} induces the stabilization of the tetragonal phase probably due to its substitutional incorporation in the $BiVO_4$ lattice. The occurrence of the Yb^{3+},Er^{3+} co-doped monoclinic-tetragonal $BiVO_4$ heterostructure induces the higher photocatalytic activities. The best photocatalytic performance was attained for the sample with 1:4 Er^{3+}:Yb^{3+} ratio. The observed NIR photoactivity clearly denotes the occurrence of an up-conversion mechanism involved in the overall photocatalytic process.

1. Introduction

The recent research activity within heterogeneous photocatalysis is focused in the development of novel alternative materials to traditional TiO_2 capable to use of sunlight as the green energy source [1,2]. In this sense, bismuth vanadate (m-$BiVO_4$) has been found to be a promising candidate used as well as in water splitting and organic contaminants decomposition under visible-light irradiation [3,4]. From different studies reported it has been stated that the properties of $BiVO_4$ are strongly dependent on its morphology and microstructure [5,6]. In this sense, the best visible-light-driven photocatalytic performance was achieved for monoclinic $BiVO_4$. This is due to the effective hybridization of Bi *6s* with O *2p* to form the valence band leading to a narrower band gap (ca. 2.4 eV) with respect to the tetragonal $BiVO_4$ one (ca. 3.0 eV). This band configuration allows extending the absorption to the visible range.

A novel challenging approach to the visible light efficient utilization would consist on the assembly of the photocatalytic material with a luminescence material [7–10]. The mechanism involved within this complex configuration is based on increasing the number of incoming radiation photons absorbed by the photocatalyst provided by the luminescence emission. Thus, an up-converting luminescent material would absorb low energy radiation from visible or Near-IR (NIR) and emit higher energy radiation (i.e. in the visible and/or UV). Several examples of this cooperative photocatalytic-luminescence mechanism have been successfully reported [11–14]. We have also stated that Er^{3+}-doping on $BiVO_4$ clearly stabilizes the tetragonal structure, subsequently exalting the luminescence properties of this material [15]. A tentative supportive mechanism has been proposed. From those results, we proposed that the presence of Er^{3+} doping into TiO_2 as host matrix favors a double mechanism, under UV and NIR excitation.

In the present paper, we describe the substantial improvement obtained by Yb^{3+},Er^{3+} co-doping for *MB* degradation and O_2 evolution reactions. The combination of these two lanthanides ions with specific incidence over the structural, electronic and luminescence features of the photocatalyst clearly affects the final photocatalytic activity. The correlation between different structural and electronic techniques with the photoactivities under different irradiation conditions would provide a possible explanation about the role of this co-doping.

2. Experimental

2.1. Samples preparation

The $BiVO_4$ samples were prepared by a hydrothermal method. First, 5 mmol of $Bi(NO_3)_3{\cdot}5H_2O$ (Sigma-Aldrich, ≥98.0%) were dissolved in 10 mL of glacial acetic acid at room temperature. Then, the stoichiometric amount of $Er(NO_3)_3$ and $Yb(NO_3)_3$ was also

* Corresponding author. Tel.: +34 954489536.
E-mail address: gcolon@icmse.csic.es (G. Colón).

0926-3373/$ – see front matter © 2014 Elsevier B.V. All rights reserved.
http://dx.doi.org/10.1016/j.apcatb.2014.01.054

dissolved in this bismuth solution. While the amount of erbium was fixed at 0.75 at%, ytterbium loading varies from 1:1 to 1:10 Er:Yb ratio. A second aqueous solution was prepared by dissolving the corresponding stoichiometric amount of NH_4VO_3 (Sigma-Aldrich, ≥99.0%) in 60 mL of hot distilled water. Afterwards, the ammonium metavanadate solution was added to the lanthanide-bismuth nitrate aqueous solution and the process was accompanied with a vigorous stirring. The pH of the obtained suspension was adjusted to 9.0 by adding concentrated NH_4OH (13 mol L^{-1}). The slurry was encased in a Teflon vessel and heated in oven at 140 °C for 20 h. The obtained precipitate was then cooled until room temperature, filtered and repeatedly washed and dried overnight at 120 °C. Afterwards, thus obtained samples were submitted to a further calcination treatment at 300 °C for 2 h.

2.2. Materials characterization

BET surface area and porosity measurements were carried out by N_2 adsorption at 77 K using a Micromeritics 2010 instrument.

X-ray diffraction (XRD) patterns were obtained using a Siemens D-501 diffractometer with Ni filter and graphite monochromator. The X-ray source was Cu Kα radiation (0.15406 nm). Rietveld analyses were performed by using XPert HighScore Plus software over selected samples. The diffraction patterns were recorded from 2θ 10° to 120° with step of 0.017° and 400 s per step.

Micro-Raman measurements were performed using a LabRAM Jobin Yvon spectrometer equipped with a microscope. Laser radiation (λ = 532 nm) was used as excitation source at 5 mW. All measurements were recorded under the same conditions (2 s of integration time and 30 accumulations) using a 100× magnification objective and a 125 mm pinhole.

The morphology of samples was followed by means of field emission-SEM (Hitachi S 4800). The samples were dispersed in ethanol using an ultrasonicator and dropped on a copper grid.

UV–vis spectra (Shimadzu, AV2101) were recorded in the diffuse reflectance mode (R) and transformed to a magnitude proportional to the extinction coefficient (K) through the Kubelka–Munk function, $F(R\infty)$. Samples were mixed with $BaSO_4$ that does not absorb in the UV–vis radiation range (white standard). Scans range was 240–800 nm.

The excitation and emission spectra of the catalysts were recorded at ambient temperature in a Horiba Jobin-Yvon Fluorolog3 spectrofluorometer operating in the front face mode operating with a 1.5 nm slit. The up-conversion optical measurements were performed for powdered pressed samples using a Jenoptik laser diode source at 980 nm. The resulting luminescence was dispersed by using an ARC Spectrapro 500-I monochromator and then detected with a photomultiplier tube.

2.2.1. Photocatalytic experimental details

Methylene Blue (*MB*) oxidation reactions were performed using a batch reactor (250 mL) using an arc lamp source (Oriel Instruments) equipped with an Hg-Xe lamp of 200 W. In the oxidation tests, an oxygen flow was employed as to produce a homogenous suspension of the catalyst in the solution. Before each experiment, the catalysts (1 g L^{-1}) were settled in suspension with the *MB* solution (150 mL) for 15 min. The evolution of the initial *MB* concentration (ca. 10 ppm) was followed through the evolution of the characteristic 664 nm band using a centrifuged aliquot ca. 2 mL of the suspension (microcentrifuge Minispin, Eppendorf). Reaction rates were calculated assuming a first order kinetic. In order to distinguish the different contributions of the different ranges of the lamp spectrum, visible and NIR photocatalytic experiments were performed. Thus for visible photocatalytic runs UV (λ < 420 nm) and IR (λ < 800 nm) cut-off filters were employed. Additionally, for NIR experiments, we use a 150 W IR lamp (Philips PAR38). The intensity of the incident UVA and visible light on the solution was measured with an HD2302 photometer (Delta OHM) using LP 471 UVA and LP 471 RAD sensors (spectral responses 315–400 nm and 400–1050 nm, respectively). The intensity of the lamp under different irradiation conditions is summarized in Table 1.

Table 1
Lamp irradiance (W/m^2) for different lamps used in the photocatalytic experiments.

Luxometer sensor	200 W Xe lamp		150 W IR lamp
	UV–vis–IR	Visible	
LP471 UVA (315–400 nm)	83	0.2	0.2
LP471 RAD (400–1050 nm)	542	170	1140

The photocatalytic activities of the samples were also evaluated for the oxygen evolution reaction from water in an $AgNO_3$ aqueous solution (0.02 M). The reaction media was continuously thermostated at 23–25 °C to prevent any significant evaporation of the solvent and discard any eventually temperature effect. The catalyst suspension (1 g L^{-1}) was firstly degassed with an N_2 stream (150 mL min^{-1}) for 30 min. After that the N_2 flow was settled at 15 mL min^{-1} and stabilized for 15 min. This nitrogen flow was used to displace the oxygen produced from the photoreactor headspace towards the GC measuring system. Then, the lamp (200 W Hg-Xe lamp, Oriel Instruments) was switched on and the effluent gases were analyzed to quantify O_2 production by gas chromatography (Agilent 490 micro GC) using a thermal conductivity detector connected to a Molsieve 5 A and Pora-PLOT Q columns.

3. Results and discussion

The structural information derived from the XRD patterns states that the initial monoclinic structure of $BiVO_4$ (*PDF* 75-1866) changes to a phase mixture when erbium is incorporated. Other phases such as $ErVO_4$ or $YbVO_4$ have not been detected. The stabilization of the tetragonal phase (*PDF* 14-0133) upon erbium doping was already reported in previous papers [15,16]. Moreover, the incorporation of different ytterbium amounts induces to an additional appearance of the tetragonal scheelite structure (Fig. 1a). From these results we can state that upon Yb^{3+},Er^{3+} doping a clear monoclinic to tetragonal transformation is taking place, being this later the predominant one as Er^{3+}:Yb^{3+} ratio is higher than 1:2 (Fig. 1b). At the same time, it is worthy to note that increasing the doping level a progressive decrease in the crystallite size is observed, which is in accordance with the tetragonal stabilization (Fig. 1c).

From Rietveld analysis it can be also pointed that the tetragonal cell is strongly affected by ytterbium incorporation (Table 2). This fact was already stated for Y^{3+} and Er^{3+} doping [15,17]. Thus, by following the evolution of the tetragonal cell parameters and volume, it can be noted that the tetragonal cell suffers a progressive contraction with increasing Yb^{3+} content. As a result, and taking into account the difference in ionic radii of bismuth and ytterbium (117 pm vs. 101 pm, respectively) [18], ytterbium incorporation would be achieved by considering the substitution of these doping ions in bismuth positions. On this basis, once the tetragonal phase is favored by lanthanides presence, both erbium and ytterbium ions would naturally occupy the Bi^{3+} positions.

The Raman spectra of Yb^{3+},Er^{3+} co-doped $BiVO_4$ also support the monoclinic to tetragonal phase transition as Yb^{3+} ratio increases (Fig. 2). Thus, it can be noticed the appearance of the ν_s(V–O) located at ca. 850 cm^{-1} corresponding to the tetragonal phase close to the band at 820 cm^{-1} assigned to the monoclinic one. Additionally, the disappearance of the $\delta(VO_4^{3-})$ doublet of the monoclinic phase is also an evidence of this phase transition. The occurrence of Er^{3+} ion favors the appearance of strong luminescence

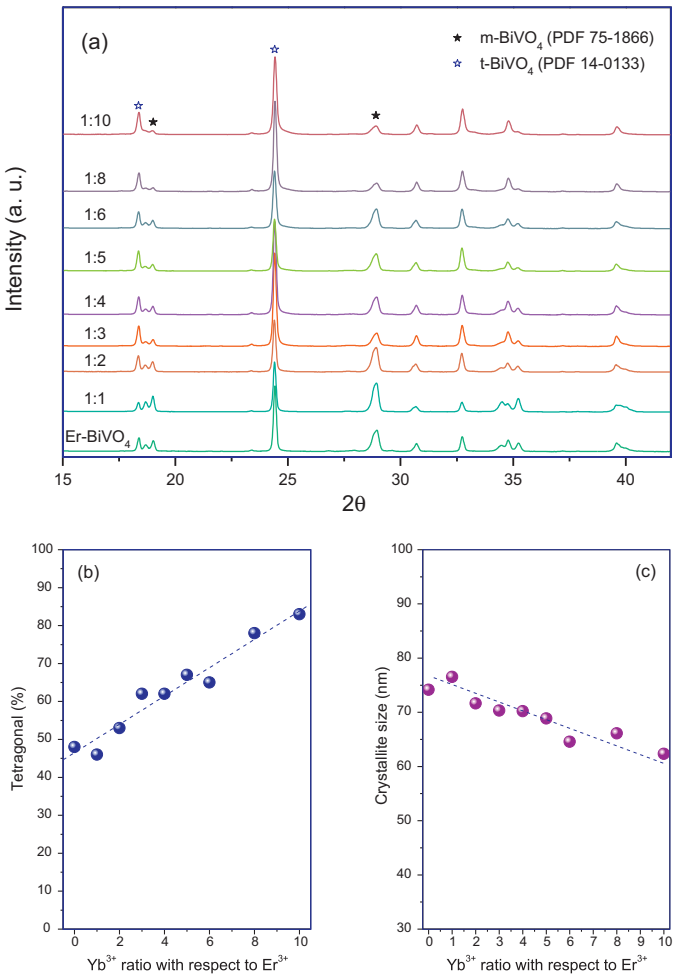

Fig. 1. (a) XRD patterns for $BiVO_4$ and Yb^{3+},Er^{3+}-codoped $BiVO_4$ obtained by hydrothermal synthesis at 140 °C; (b) Evolution of the tetragonal phase; and (c) Evolution of the tetragonal crystallite size with Yb^{3+} ratio.

band upon Raman laser excitation at 532 nm [15]. As ytterbium is incorporated, in addition to the above structural evolution toward the tetragonal phase the increasing of the luminescence emission intensity is observed. This fact would support the favorable effect of ytterbium on erbium luminescence properties [19].

In accordance to literature, surface area values obtained for $BiVO_4$ and doped $BiVO_4$ are significantly low (Table 2) [20]. However, as overall Ln^{3+} doping increases a slight increase in surface area is observed.

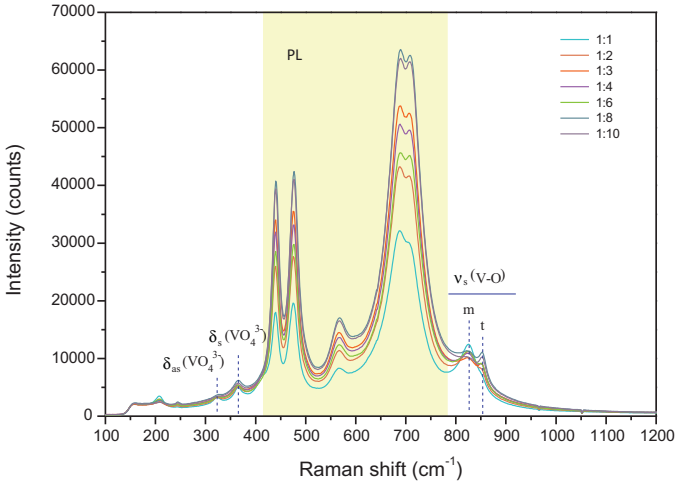

Fig. 2. Raman spectra for $BiVO_4$ and Yb^{3+},Er^{3+}-codoped $BiVO_4$ obtained by hydrothermal synthesis at 140 °C.

The progressive appearance of the tetragonal phase also has a significant effect on the absorption properties of the system. As it is widely stated, m-$BiVO_4$ presents an absorption band within the visible range while t-$BiVO_4$ shows an absorption edge just in the limit between UV and visible range (Fig. 3). So, the occurrence of this structure leads to the decrease of the visible absorption band that remains as a shoulder of t-$BiVO_4$ spectrum. This evolution corroborates the monoclinic to tetragonal structure transition observed from the diffraction patterns as ytterbium content is increased. In addition to the $BiVO_4$ absorption profile, doped systems show small absorption bands in the range 500–700 nm which can be associated to the excitation of Er^{3+} species (Inset in Fig. 3) [14,21]. These absorption lines located at 520 nm and 653 nm would correspond to the transitions from the Er^{3+} ground state $^4I_{15/2}$ to the higher energy levels $^4H_{11/2}$ and $^4F_{9/2}$, respectively [15]. The calculated band gap values are summarized in Table 2, and are in accordance with the monoclinic and tetragonal reported in the literature [22].

The morphology of $BiVO_4$ has been extensively reported to be dependent on the preparation route [23–25]. In our case, bare m-$BiVO_4$ shows a rod-like morphology (Fig. 4a). As lanthanide ions are incorporated, the morphology of the sample clearly denotes the mixture of the two phases present (Fig. 4b). Moreover, the initial rod-like particles develop to a well-defined prism-like morphology typical for monoclinic structure [24]. Additionally other needle-like particles are present that could be ascribed to tetragonal $BiVO_4$. With Yb^{3+} content increasing the presence of prism-like particles associated to the monoclinic phase tends to disappear (Fig. 4c–f).

Table 2
Surface, structural and photocatalytic characterization for $BiVO_4$ and Er^{3+}, Yb^{3+} codoped $BiVO_4$ catalysts.

Samples	Er:Yb ratio	Cell parameters[a]		Cell Volume[a] (Å^3)	BET (m^2/g)	Band gap (eV)		O_2 evolution Rate (μmol/g h)
		a = *b*	*c*			M	T	
m-$BiVO_4$		–	–	–	<1	2.38	–	58
t-$BiVO_4$		7.304 (7)	6.461 (3)	344.7	6	–	2.70	37
Er-$BiVO_4$[b]		7.303 (0)	6.460 (0)	344.5	<1	2.33	2.67	320
Yb-Er-$BiVO_4$[b]	1:1	7.301 (7)	6.459 (3)	344.4	1	2.33	2.63	360
	1:2	7.301 (6)	6.459 (3)	344.4	2	2.33	2.68	–
	1:3	7.302 (0)	6.459 (4)	344.4	3	2.33	2.68	–
	1:4	7.301 (7)	6.459 (0)	344.4	4	2.35	2.68	435
	1:5	7.301 (8)	6.458 (7)	344.3	6	2.34	2.62	–
	1:6	7.301 (5)	6.458 (1)	344.3	5	2.34	2.61	390
	1:8	7.300 (9)	6.457 (8)	344.2	5	2.35	2.68	–
	1:10	7.300 (2)	6.457 (2)	344.1	7	2.35	2.85	–

[a] Structural parameters for tetragonal phase.
[b] Er content = 0.75 at%.

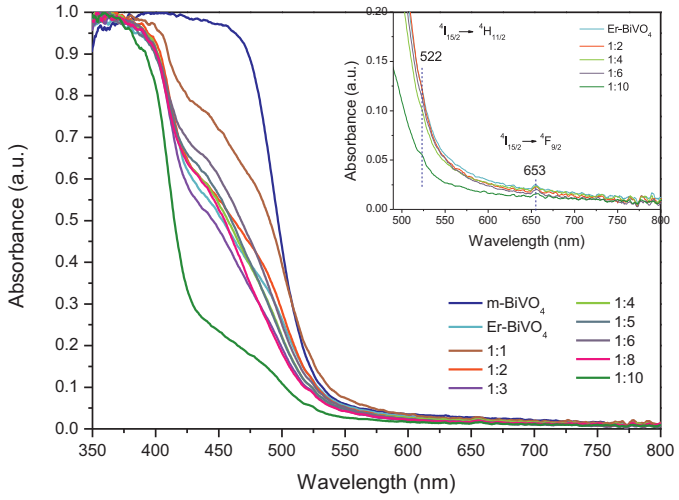

Fig. 3. Diffuse reflectance spectra for $BiVO_4$ and Yb^{3+},Er^{3+} codoped systems obtained by hydrothermal synthesis at 140 °C.

To study the photocatalytic activities of $BiVO_4$ doped systems, *MB* degradation and O_2 evolution reactions have been followed. In Fig. 5 we show the photocatalytic activity of the studied systems for the photodegradation reaction. We have already reported the significant improvement of erbium doping on the $BiVO_4$ photocatalytic activity [16]. As it can be observed from Fig. 5a, the progressive incorporation of ytterbium ion into the Er^{3+}-$BiVO_4$ structure produces a clear additional enhancement in the *MB* photodegradation. Thus, the best photocatalytic performance was achieved for an Er^{3+} to Yb^{3+} ratio of 1:4. As ytterbium loading is higher than this ratio the reaction rate progressively decays (Fig. 5b). From this plot it is clear that besides the increase of surface area values observed for co-doped $BiVO_4$, the particular structural features of the systems might be the reason of the photocatalytic activity enhancement. In this sense, t-$BiVO_4$ reference sample which exhibits similar surface area values as co-doped systems, does not achieve by far the conversion values reached for those later systems. As it has been reported, the monoclinic-tetragonal heterostructured $BiVO_4$ is expected to promote the separation of photoinduced electron–hole pairs [17,26]. On this basis, we could state that in principle the conjunction of morphological and structural features clearly provides better photocatalytic performance.

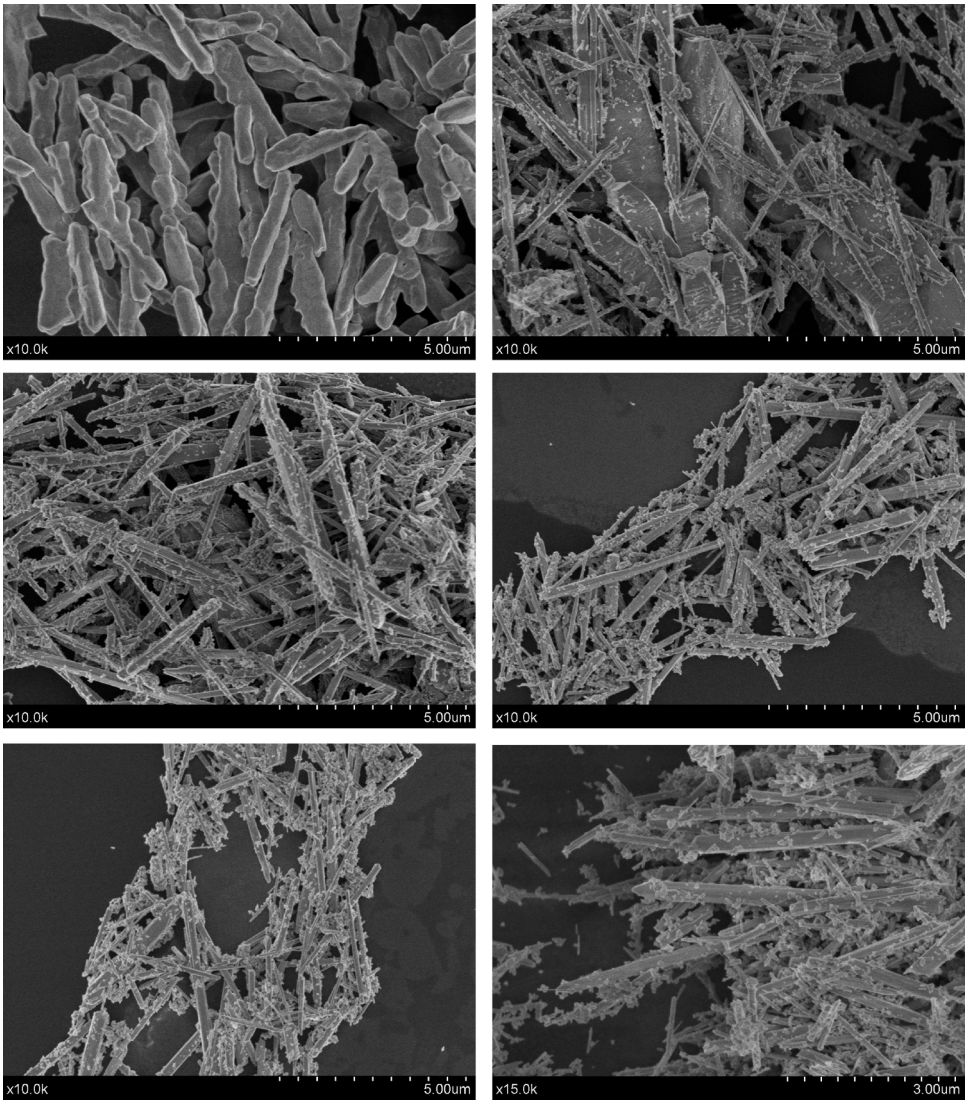

Fig. 4. SEM images of (a) m-$BiVO_4$; (b) Yb^{3+},Er^{3+}-$BiVO_4$ 2:1; (c) Yb^{3+},Er^{3+}-$BiVO_4$ 4:1; (d) Yb^{3+},Er^{3+}-$BiVO_4$ 6:1; (e) Yb^{3+},Er^{3+}-$BiVO_4$ 8:1; (f) Yb^{3+},Er^{3+}-$BiVO_4$ 10:1.

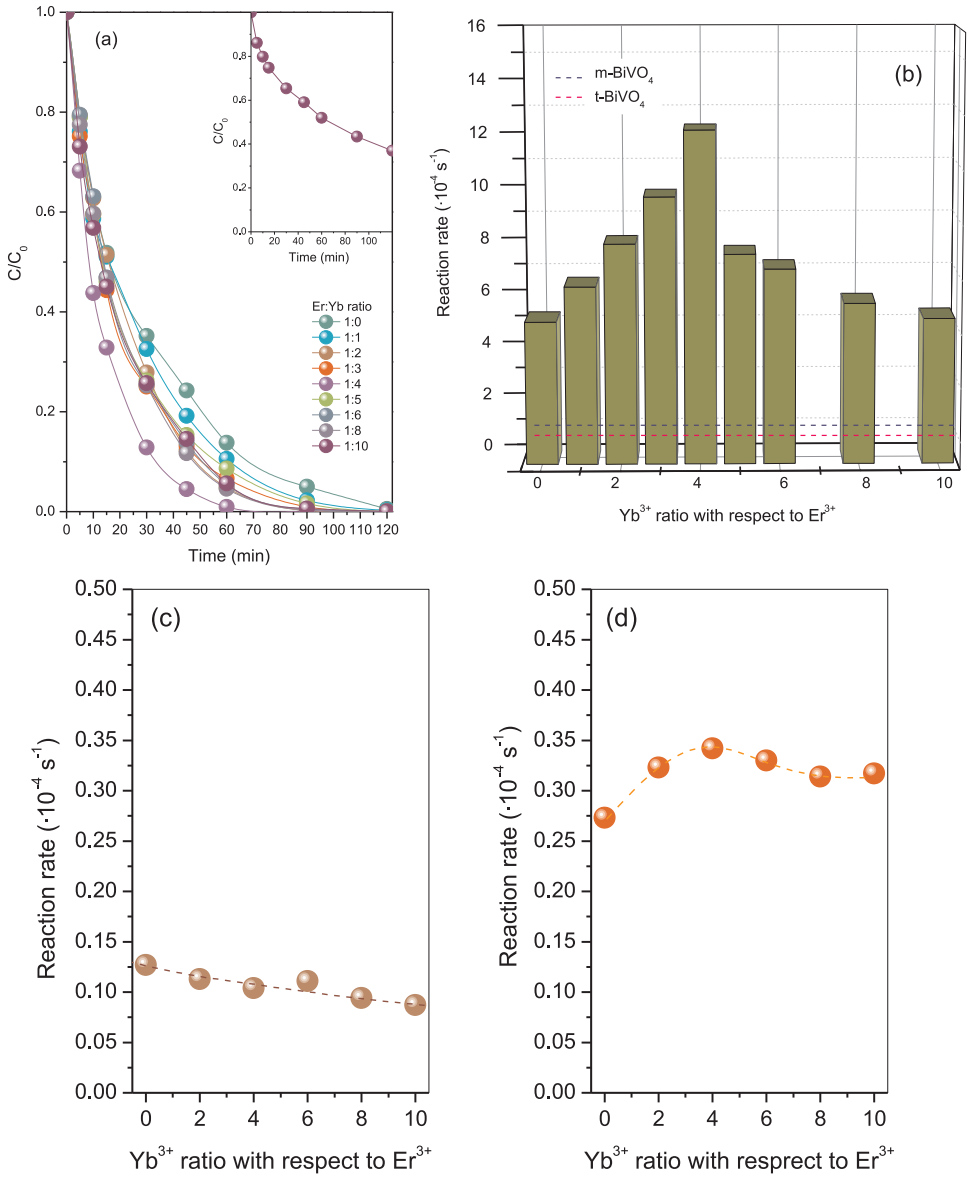

Fig. 5. Photocatalytic activity of different for $BiVO_4$ and Yb^{3+},Er^{3+}-codoped $BiVO_4$ catalysts for *MB* degradation reaction. (a) Evolution of *MB* concentration with irradiation time under ˛UV–vis–NIR range; (b) Calculated reaction rates for different ytterbium content on Yb^{3+},Er^{3+}-$BiVO_4$ from Fig. 5a conversion plot. (c) Calculated reaction rates for different ytterbium content on Yb^{3+},Er^{3+}-$BiVO_4$ upon visible range light (Reaction rates for pristine $BiVO_4$: m-$BiVO_4$ = 0.407×10^{-4} s^{-1} and t-$BiVO_4$ = 0.045×10^{-4} s^{-1}). (d) Calculated reaction rates for different ytterbium content on Yb^{3+},Er^{3+}-$BiVO_4$ upon NIR range light (Reaction rates for pristine $BiVO_4$: m-$BiVO_4$ = 0.031×10^{-4} s^{-1} and t-$BiVO_4$ = 0.035×10^{-4} s^{-1}).

In order to elucidate in deep the specific role of ytterbium and erbium on the reaction mechanism besides the structural effects, we have performed the degradation reaction under visible and NIR irradiation conditions (Fig. 5c and d). As expected, under visible irradiation m-$BiVO_4$ shows the best photocatalytic performance while t-$BiVO_4$ shows a negligible photoactivity (Fig. 5c). Moreover, the photoactivities under visible irradiation clearly decay as Yb^{3+} relative ratio increases. This evolution can be explained by considering the progressive tetragonal phase stabilization taking place as Yb^{3+} content increases. The fraction of the visible-active monoclinic phase gradually decays and therefore the photocatalytic performance diminishes. Therefore, the upgraded photoactivity observed by heterostructured $BiVO_4$ cannot be considered in this case. This would also imply that the monoclinic-tetragonal heterojunction functions adequately when tetragonal phase is excited by UV photons. Then, considering the relative positions of the conduction and valence bands for both structures, it can be assumed that the photogenerated holes in the tetragonal structure can be driven towards the valence band of the monoclinic one increasing the photoefficiency of the process.

If we observe the evolution of the reaction rates under NIR illumination (Fig. 5d) it is worthy to note that, as expected, neither m-$BiVO_4$ nor t-$BiVO_4$ show significant photoactivities (ca. 0.03×10^{-4} s^{-1} in both cases vs ca. 0.3×10^{-4} s^{-1} for codoped $BiVO_4$). On the other hand, the co-doped systems exhibit higher photoactivities under NIR than under visible illumination. Since no NIR photon absorption by $BiVO_4$ is expected, the occurrence of an additional process involved in the overall mechanism might be considered. Bearing in mind that an up-conversion process would imply the transformation of low energy NIR photons to higher energy one (visible or UV), it can be assumed that under NIR irradiation conditions erbium and ytterbium ions would participate in such process by emitting visible or UV photons. As it can be seen, as ytterbium relative ratio increases the reaction rate upon

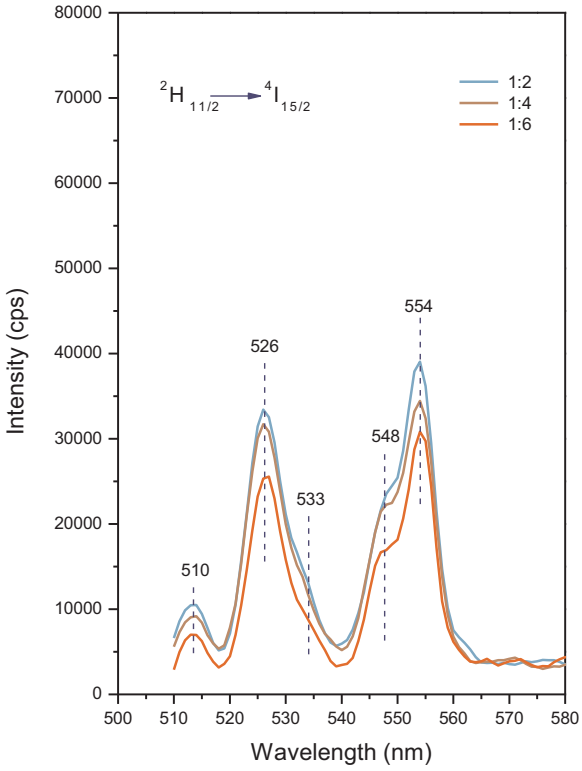

Fig. 6. Up-conversion emission spectra of Yb^{3+},Er^{3+} co-doped $BiVO_4$ upon 980 nm excitation corresponding to the $^2H_{11/2} \rightarrow {}^4I_{15/2}$ transition.

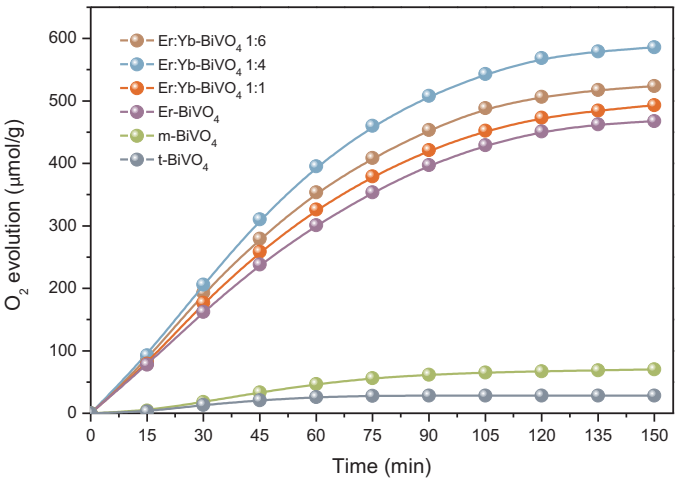

Fig. 7. Photocatalytic O_2 evolution for Yb^{3+},Er^{3+} co-doped $BiVO_4$ samples from aqueous $AgNO_3$ solutions (0.02 mol L^{-1}) under full lamp spectrum excitation as a function of the irradiation time.

NIR irradiation increases reaching a maximum value for 1:4 erbium to ytterbium ratio. For higher ytterbium loadings the reaction rate slightly decays. Consequently, the existence of these simultaneous processes (photocatalytic and luminescent) would favor the overall efficiency under UV–vis–NIR irradiation conditions.

In order to confirm the above discussion, the up-conversion photoluminescence spectra of ytterbium-erbium co-doped systems were recorded. In Fig. 6 we show the room temperature PL spectra upon excitation at 980 nm for selected samples. All systems exhibit clear emission bands in the 500–700 nm range, with two clear contributions located at 526 and 554 nm. This double emission band was already described for different authors and has been associated to the green $^2H_{11/2}$-$^4I_{15/2}$ and red $^4F_{9/2} \rightarrow {}^4I_{15/2}$ transitions [27,28]. As it can be observed, the intensities for the bands located within this range appear similar for the three Yb^{3+}-Er^{3+} $BiVO_4$ samples studied. This would imply that the monoclinic $BiVO_4$ phase would effectively absorb photons in this range. As monoclinic phase fraction decrease with ytterbium incorporation the photon harvesting would also decrease buffering the up-conversion emission spectrum for each sample. Furthermore, no emission bands have been detected below 500 nm. Thus, the weak violet emission located at ca. 420 nm ($^2H_{9/2} \rightarrow {}^4I_{15/2}$ transition) reported for Yb^{3+},Er^{3+} luminescent systems was not observed in our case [29]. The absence of such emission band can be explained by assuming an extremely weak emission in our system which not allow its detection and/or even considering the effective absorption by tetragonal $BiVO_4$.

Finally, in Fig. 7 it is shown the photocatalytic water oxidation activity of different Yb^{3+},Er^{3+} co-doped $BiVO_4$ samples from an aqueous solution containing $AgNO_3$ as a sacrificial reagent under sunlight irradiation. As Yb^{3+} relative ratio increases the photoactivity for O_2 progressively increases (Table 2), reaching a maximum O_2 evolution rate for erbium to ytterbium ratio of 1:4 (435 μmol h^{-1} g^{-1}), which is more than 8 times of that of bare m-$BiVO_4$ (53 μmol h^{-1} g^{-1}). It is worthy to mention that O_2 evolution seems to be stopped after 90 min of reaction (Fig. 6). This is probably due to Ag cluster formation in the reactor walls that would shield the incident light coming from outside of the reactor. Indeed, this detrimental point was already highlighted by Ke et al. [17,30] From the O_2 evolution reaction results, it is clear that these materials appear as a patent candidate for water splitting reaction.

4. Conclusions

We have obtained a highly active monoclinic-tetragonal $BiVO_4$ heterostructured system by doping with Yb^{3+} and Er^{3+}. From the structural and surface analysis the incorporation of Er^{3+} can be stated. From the photocatalytic experiments we tentatively propose a double mechanism which could explain the improved photoactivities in doped systems. On one hand, the lanthanide doping would favor the coexistence of a monoclinic-tetragonal heterostructure. Such structural configuration would provide improved photocatalytic efficiency by optimizing the charge separation. Secondly, Yb^{3+},Er^{3+} luminescence tandem would lead to a supportive photoluminescence up-conversion process. Thus, it can be evidenced a small contribution of NIR photons in the overall mechanism due an energy transfer process from erbium ions to the monoclinic phase $BiVO_4$. On this basis, we propose a $BiVO_4$ based catalysts photocatalytically active in the overall range of light spectrum.

Acknowledgements

The financial support by projects *P09-FQM-4570* and *ENE2011-24412* is fully acknowledged. S. Obregón Alfaro thanks CSIC for the concession of a JAE-Pre grant.

References

[1] M. Maeda, K. Domen, J. Phys. Chem. C 111 (2007) 7851–7861.
[2] A. Kubacka, M. Fernández-García, G. Colón, Chem. Rev. 112 (2012) 1555–1614.
[3] A. Kudo, K. Omori, H. Kato, J. Am. Chem. Soc. 121 (1999) 11459–11467.
[4] Y. Park, K.J. McDonald, K.S. Choi, Chem. Soc. Rev. 42 (2013) 2321–2337.
[5] S. Tokunaga, H. Kato, A. Kudo, Chem. Mater. 13 (2001) 4624–4628.
[6] L. Zhou, W. Wang, L. Zhang, H. Xu, W. Zhu, J. Phys. Chem. C 111 (2007) 13659–13664.
[7] Z. Zhang, W. Wang, J. Xu, M. Shang, J. Ren, S. Sun, Catal. Comm. 13 (2011) 31–34.

[8] T. Zhou, J. Hu, J. Li, Appl. Catal. B: Environ. 110 (2011) 221–230.
[9] Z.X. Li, F.B. Shi, T. Zhang, H.S. Wu, L.D. Sun, C.H. Yan, Chem. Comm. 47 (2011) 8109–8111.
[10] Y. Tang, W. Di, X. Zhai, R. Yang, W. Qin, ACS Catal. 3 (2013) 405–412.
[11] W. Qin, D. Zhang, D. Zhao, L. Wang, K. Zheng, Chem. Comm. 46 (2010) 2304–2306.
[12] T. Li, S. Liu, H. Zhang, E. Wang, L. Song, P. Wang, J. Mater. Sci. 46 (2011) 2882–2886.
[13] S. Obregón, G. Colón, Chem. Comm. 48 (2012) 7865–7867.
[14] S. Obregón, A. Kubacka, M. Fernández-García, G. Colón, J. Catal. 299 (2013) 298–306.
[15] S. Obregón, G. Colón, Dalton Trans. 43 (2014) 311–326.
[16] S. Obregon, G. Colón, under revision.
[17] S. Usai, S. Obregón, A.I. Becerro, G. Colón, J. Phys. Chem. C 117 (2013) 24479–24484.
[18] R.D. Shannon, Acta Cryst. 32 (1976) 751–767.
[19] J. Liao, Z. Yang, H. Wu, D. Yan, J. Qiu, Z. Song, Y. Yang, D. Zhou, Z. Yin, J. Mater. Chem. C 1 (2013) 6541–6546.
[20] H. Jiang, H. Dai, X. Meng, K. Ji, L. Zhang, J. Deng, Appl. Catal. B: Environ. 105 (2011) 326–334.
[21] G. Wang, W. Qin, J. Zhang, J. Zhang, Y. Wang, C. Cao, L. Wang, G. Wei, P. Zhu, R. Kim, Opt. Mater. 31 (2008) 296–299.
[22] S. Tokunaga, H. Kato, A. Kudo, Chem. Mater. 13 (2001) 4624.
[23] Z. Wang, W. Luo, S. Yan, J. Feng, Z. Zhao, Y. Zhu, Z. Li, Z. Zou, CrystEngComm 13 (2011) 2500–2504.
[24] S. Obregón, A. Caballero, G. Colón, Appl. Catal. B: Environ. 117–118 (2012) 59–66.
[25] J. Sun, G. Chen, J. Wu, H. Dong, G. Xiong, Appl. Catal. B: Environ. 132–133 (2013) 304–314.
[26] H. Fan, T. Jiang, H. Li, D. Wang, L. Wang, J. Zhai, D. He, P. Wang, T. Xie, J. Phys. Chem. C 116 (2012) 2425–2430.
[27] V. Mahalingama, C. Hazraa, R. Naccacheb, F. Vetroneb, J.A. Capobianco, J. Mater. Chem. C 1 (2013) 6536–6540.
[28] X. Huang, S. Han, W. Huang, X. Liu, Chem. Soc. Rev. 42 (2013) 173–201.
[29] F. Wang, X. Liu, J. Am. Chem. Soc. 130 (2008) 5642–5643.
[30] D. Ke, T. Peng, L. Ma, P. Cai, P. Jiang, Appl. Catal. A: Gen. 350 (2008) 111–117.